batteries

MDPI

Article

Multi-Layer TiO_{2-x}-PEDOT-Decorated Industrial Fe_2O_3 Composites as Anode Materials for Cycle-Performance-Enhanced Lithium-Ion Batteries

Yangzhou Ma [1,2], Qi Li [1], Haoduo Li [1], Zhenfei Cai [1], Shuai Wang [1], Li Zhang [1], Jian Li [1], Guangsheng Song [1,*], Youlong Xu [2,*] and Tingfeng Yi [3]

1 Key Laboratory of Green Fabrication and Surface Technology of Advanced Metal Materials, Ministry of Education, School of Materials Science and Engineering, Anhui University of Technology, Maanshan 243002, China; yangzhou.ma@outlook.com (Y.M.); liqi855@163.com (Q.L.); m18691685169@163.com (H.L.); zhenfei_cai@163.com (Z.C.); ws_ahut@163.com (S.W.); zhangli1@etcbattery.com (L.Z.); jianli13625593904@outlook.com (J.L.)

2 Electronic Materials Research Laboratory, Key Laboratory of the Ministry of Education, Xi'an Jiaotong University, Xi'an 710049, China

3 School of Resources and Materials, Northeastern University at Qinhuangdao, Qinhuangdao 066004, China; yitingfeng@neuq.edu.cn

* Correspondence: song_ahut@163.com (G.S.); ylxu@mail.xjtu.edu.cn (Y.X.)

Abstract: An industrial submicron-sized Fe_2O_3 with no special shape was decorated by a multi-layer coating of oxygen-deficient TiO_{2-x} and conducting polymer PEDOT (poly 3,4-ethylenedioxythiophene). A facile sol–gel method followed by an EDOT polymerization process was adopted to synthesize the hierarchical coating composite. The microstructure and phase composition were characterized using an X-ray diffraction analysis (XRD), scanning electron microscopy (SEM), and transmission electron microscopy (TEM). In particular, the existence state of PEDOT was determined using Fourier transform infrared (FT-IR) and a thermogravimetric (TG) analysis. The characterization results indicated the dual phase was well-coated on the Fe_2O_3 and its thickness was nano scale. Electrochemical characterization indicated that the multi-layer coating was helpful for significantly enhancing the cycle stability of the Fe_2O_3, and its electrochemical performance was even better than that of the single-layer coating samples. The synergistic effects of the ceramic phase and conducting polymer were demonstrated to be useful for improving electrochemical properties. The obtained FTP-24 sample exhibited a specific discharge capacity of 588.9 mAh/g after 360 cycles at a current density of 100 mA/g, which effectively improved the intrinsic cycling performance of the Fe_2O_3, with a corresponding discharge capacity of 50 mAh/g after 30 cycles.

Keywords: Fe_2O_3; TiO_{2-x}-PEDOT; multi-layer coating; anode material; high stability; Li-ion batteries

check for updates

Citation: Ma, Y.; Li, Q.; Li, H.; Cai, Z.; Wang, S.; Zhang, L.; Li, J.; Song, G.; Xu, Y.; Yi, T. Multi-Layer TiO_{2-x}-PEDOT-Decorated Industrial Fe_2O_3 Composites as Anode Materials for Cycle-Performance-Enhanced Lithium-Ion Batteries. *Batteries* **2023**, *9*, 481. https://doi.org/10.3390/batteries9090481

Academic Editor: Elie Paillard

Received: 23 August 2023
Revised: 6 September 2023
Accepted: 20 September 2023
Published: 21 September 2023

1. Introduction

Rapid development in the field of energy storage has posed higher demands on new materials, leading to the development of multiple energy storage devices and materials [1–5], such as lithium-, sodium-, and potassium-ion batteries [6–9]. Lithium-ion batteries have been widely applied on power grids, electric vehicles, and portable devices in recent years, which is due to their high energy density, cycle stability, and environmentally friendly features compared to some traditional energy storage devices [10–13]. To meet the demand of the high energy storage of Li-ion batteries, a large number of anode materials, such as silicon [14,15] and transition metal oxides [16–18] etc., have been developed to substitute graphite. Iron oxide (Fe_2O_3) has been demonstrated to be one of the most promising candidates due to its low cost, considerable specific capacity (~1000 mAh/g), and environmental friendliness [19–22]. However, the anode faces the problem of rapid capacity decay and a low Coulombic efficiency,

which is due to its large volume expansion during cycling, particle agglomeration, and the inherently low electrical conductivity of the metal oxide.

Coating is the most direct and effective strategy for overcoming these problems [23–26]. Buffered and high-ionic/electronic-conductivity materials can be introduced on the surfaces of Fe_2O_3 particles to prolong their cycling life, inhibit particle agglomeration, and ensure fast Li-ion diffusion [27–30]. Carbon, metal oxides, and conductive polymers, as the most frequent coating materials, have been introduced to Fe_2O_3-based composites. All coating materials should be modified for better application as anode materials, for example, Fe_2O_3 nanoparticles anchored on N-doped carbon remained at 496 mAh g^{-1} after 1000 cycles at 500 mA g^{-1}, which effectively suppressed the electrode pulverization [31]. Multi-layer, yolk-shell structured Fe_2O_3@carbon was designed to prolong the cycle life, which possessed a high charge capacity of 800.6 mAh g^{-1} after 300 cycles at 4 A g^{-1}. Meanwhile, the phase and structural evolution was uncovered by in situ TEM measurements, and the improved structural properties of multiple layers contributed to the enhancement of battery performance [32]. Oxides are more likely to be used as coating materials due to their better Li-ion conductivity. TiO_2 has attracted much attention among various oxide candidates due to it having a higher ionic conductivity than amorphous carbon and an excellent electrochemical stability. The Fe_2O_3@TiO_2 core–shell structure has been demonstrated to be beneficial to electrochemical performance. Zeng et al. reported core–shell nanospheres with a high reversible specific capacity of 497.3 mAh g^{-1} up to 100 cycles [33]. We introduced oxygen defects into a TiO_2 coating layer to further improve its conductivity, and obtained TiO_2-coated α-Fe_2O_3 composites with a high cycling performance in our previous work [34]. Some flexible materials were adopted to be added into the Fe_2O_3-TiO_2 composites to inhibit the pulverization issue in the charge/discharge process. Fu et al. chose CNTs as the core supporting material, and coated with Fe_2O_3-TiO_2. The composites remained at a specific capacity of 770 mAh g^{-1} after 200 cycles under a current density of 200 mA g^{-1} [35]. Conductive polymers, such as polypyrrole (PPY) [36,37], polyaniline (PANI), and poly 3,4-ethylenedioxythiophene (PEDOT) [38,39] etc., were applied in energy storage devices for a long time for their long cycling performance. Jeong et al. [40] designed a hierarchical hollow spheres structure with PANI as a coating layer, and the composites exhibited an excellent rate performance and cycling stability during 100 cycles, remaining at 732 mAh g^{-1}. The electrical conductivity of the entire electrodes was increased significantly by the introduction of conductive polymers.

PEDOT possesses a better stability of ion-doped states compared to other conductive polymers [41]. It has been demonstrated that the incorporation of PEDOT can enhance the electrochemical performance of Fe_2O_3 [42]. Based on our previous work of oxygen-deficient TiO_2-coated Fe_2O_3 composites, we adopted a PEDOT coating on the composites to further improve their electrical conductivity. The hierarchical structure was helpful for improving the α-Fe_2O_3 anode cycling stability.

2. Materials and Methods

2.1. Synthesis of Fe_2O_3/TiO_{2-x}/PEDOT Composites

The composites were synthesized via a simple polymerization method for Fe_2O_3/TiO_{2-x} composites reported in our previous study [34]. A certain amount of precursor particles, Fe_2O_3/TiO_2 with oxygen defects, were stirred and suspended in deionized water. The thickness of the PEDOT coated on the particles was regulated by the polymerization time. The EDOT monomer at 100 μL was dropped in the suspension liquid and then 0.1 g of camphorsulfonic acid (HCSA) was introduced into the mixture as a dopant. The stirring times were set as 8 h, 24 h, 40 h, and 56 h after 0.5 g of ammonium persulfate was added into the liquid. The final products were obtained with the washing and drying process, labeled as FTP-8, FTP-24, FTP-40, and FTP-56. The full synthesis process is briefly illustrated in Figure 1.

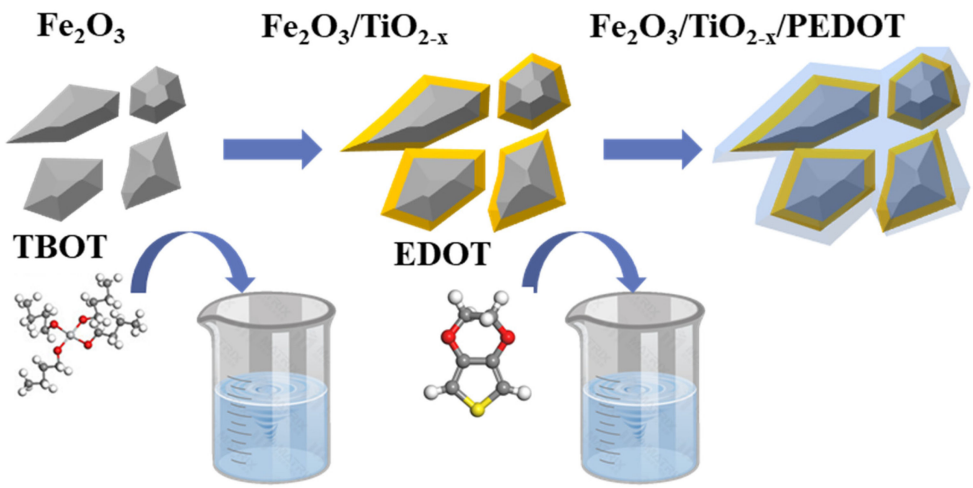

Figure 1. Schematic illustration of the preparation process of Fe_2O_3/TiO_{2-x}/PEDOT anode materials.

2.2. Characterization

The compounds' surface morphologies and distributions of elements were examined using a combination of FESEM (Field Emission Scanning Electron Microscopy; NANO SEM 430) and EDS (Energy Dispersive X-ray Spectroscopy). The composites' coating layers and lattice structures were characterized using TEM (Transmission Electron Microscopy; JEM-2100, JOEL). The powder's structural information was detected using an XRD (X-ray Diffraction) analyzer (Bruke D8), utilizing Cu-Kα radiation (λ = 1.5406 Å) within the 2θ range of 10−80°. The compounds' compositions and oxidation states were determined through XPS (X-ray Photoelectron Spectroscopy, Thermo K-Alpha+, Al Kα 1486.6 eV). The characteristic peaks of PEDOT were identified using FT-IR (Fourier Transform Infrared Spectrum) performed on a Nicolet 6700 spectrophotometer. The content of PEDOT in the mixture was quantified via a TG (Thermogravimetric) analysis conducted under air, ranging from room temperature to 900 °C, employing a DTG-60H model from Shimadzu, Kyoto, Japan.

2.3. Electrochemical Measurement

The working electrodes consisted of 80 wt% active materials, 10 wt% acetylene black, and 10 wt% CMC + citric acid mixture in deionized water, ensuring a homogeneous slurry. This slurry was then evenly applied onto a copper foil and dried in a vacuum oven at 60 °C for 24 h. Afterward, the coated electrodes were cut into disks with a diameter of 14 mm. The average mass loading of the active material in each electrode was 1.6 mg. The specific capacity calculation was based on the total mass of all the active materials present on the electrodes. To assemble the CR2016-type half-cell, a thin Li plate was utilized as the anode electrode, while Celgard 2400 served as the separator. The entire assembly process was carried out in an argon glove box (MBRAUN Unilab), with the water and oxygen levels being maintained below 0.1 ppm. Galvanostatic charge/discharge characterization was performed at room temperature using a Neware battery test system (Neware Technology Co., Ltd., Shenzhen, China). The cut-off voltage was set at 0.01−2.5 V. In order to assess the coating effect, electrochemical impedance spectroscopy (EIS) was conducted prior to the cycling test. This analysis evaluated the electronic resistance and ion diffusion rate within a frequency range from 10 mHz to 10 MHz, with a 10 mV bias. The measurements were conducted using a CS310H electrochemical workstation system (Corrtest, Co. Ltd., Wuhan, China). Furthermore, cyclic voltammetry (CV) measurements were performed with a scan rate of 0.1 $mV \cdot s^{-1}$ between 0.01 and 3.0 V in order to gather additional information.

3. Results

3.1. Structural and Physicochemical Analysis of the FTP Powders

The XRD results of the Fe_2O_3/TiO_{2-x}/PEDOT composites with various EDOT polymerization durations are shown in Figure 2a. For each sample, most of the high-intensity diffraction peaks indicated a Hematite α-Fe_2O_3 phase (ICDD#01-073-2234), which meant that the main component of the composites was the commercial Fe_2O_3. It was noted that some tiny peaks appeared at 30.2° and 57.3°, manifesting a Maghemite γ-Fe_2O_3 phase (ICDD#00-039-1346). This phase, which benefited the cycling performance, was formed along with the reduction process of the TiO_2 coating. The characteristic peaks of TiO_2 and PEDOT cannot be detected clearly in the curves; thus, the TIO_2 and PEDOT coating layer may exist in the composites as an amorphous phase, and the PEDOT-coating process had no effect on the phase structure of the Fe_2O_3/TiO_2 composites.

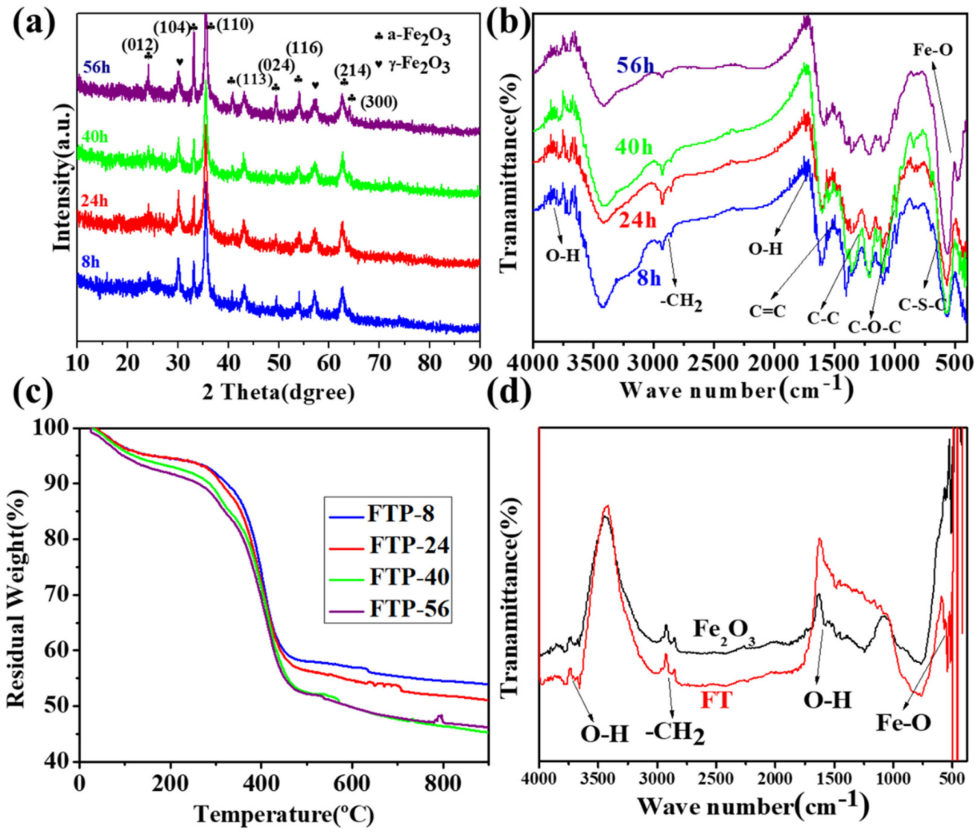

Figure 2. (**a**) XRD patterns, (**b**) FT-IR results, and (**c**) TG curves of Fe_2O_3/TiO_{2-x}/PEDOT composites with multiple polymerization times, and (**d**) FT-IR results of Fe_2O_3 and Fe_2O_3/TiO_{2-x} as control groups.

In order to confirm the existence of PEDOT in the final composites, FT-IR was performed for all the composites with multiple polymerization durations. It can be seen that the characteristic peaks of Fe_2O_3 were shown at 470 cm^{-1} (Fe-O), 2871 cm^{-1} (C-H), 3400 cm^{-1}, and 1640 cm^{-1} (O-H). Meanwhile, the characteristic peaks corresponding to PEDOT were detected at 1315 cm^{-1} (C-C), 1515 cm^{-1} (C=C), 1048 cm^{-1} (C-O-C), and 674 cm^{-1} (C-S-C). It can be demonstrated that the EDOT was well polymerized and deposited in the composites. In addition, the FTP-56 and FTP-40 samples had higher-intensity peaks at 674 cm^{-1} due to longer polymerization durations, leading to more polymer being produced. Further evidence to verify the existence of PEDOT is the FT-IR results of the pure Fe_2O_3 and Fe_2O_3 coated with TiO_2, which are illustrated in Figure 2d. The characteristic peaks corresponding to PEDOT cannot be found in the spectrum; instead, some detected peaks only corresponded to the Fe_2O_3. Thus, the PEDOT was well-added into the composites.

Figure 2c shows the TG results of the Fe_2O_3/TiO_{2-x}/PEDOT composites. The weight loss below 100 °C was due to the moisture and some oligomer in the composites. When the temperature was increased to above 350 °C, the PEDOT started combustion and the weight loss became quite significant. The weight residuals of FTP-8 to FTP-56 were 53.2%, 50.3%, 44.2%, and 45.3%, respectively. The thickness of the polymer coating layer had a positive correlation with the polymerization duration. As the polymerization duration increased, the polymerization rate slowed down. When the duration exceeded 40 h, the EDOT in the solution was used up. The content of PEDOT in FTP-40 and FTP-56 was almost the same, which led to similar electrochemical performances.

The morphology and structure information is illustrated in Figure 3. The SEM image of raw commercial Fe_2O_3 is shown in Figure 3a. The mean particle size was 2–4 µm and possessed an irregular shape. The TiO_{2-x}-coating process had slight effect on the particle size in our previous investigation [34]. However, with the PEDOT layer added into the composites, the process had a significant influence on the particle size, as shown in Figure 3b. For each PEDOT coating, the composites had a similar morphology. FTP-24 was chosen as a representative of all the FTP samples. It can be seen that the particle size increased to 10–15 µm and some secondary small particles were distributed randomly around the main particle. This can be attributed to the Fe_2O_3 particle aggregation in the EDOT polymerization process. This intricate process often begins with monomer adsorption onto the surface of iron oxide particles, followed by subsequent chemical reactions that lead to the formation of polymer chains. As a result, small particles are interconnected, giving rise to larger particles, and, consequently, an increase in particle size. Thus, the PEDOT intertwined on the Fe_2O_3 particles had a confinement effect on the particles to inhibit the expansion in the Li insertion process, which helped to improve the cycle performance. The corresponding EDS mapping results of FTP-24 are shown in Figure 3c. The main observable elements of Fe, O, and Ti were uniformly distributed, which meant the composite had no local segregation.

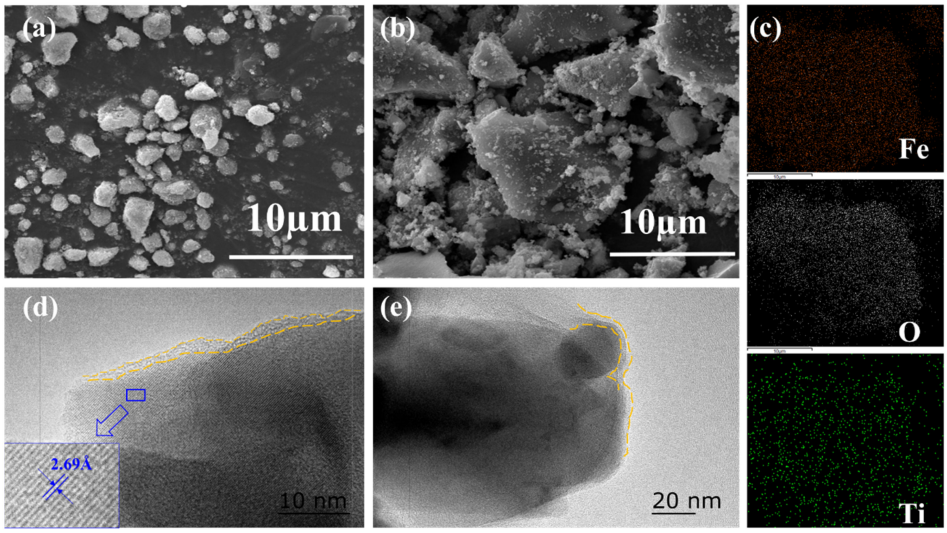

Figure 3. The morphology and structure characterization of the composites. (**a**) SEM image of raw commercial Fe_2O_3. (**b**) SEM image of FTP-24 as a representative of the PEDOT-coated composites. (**c**) The corresponding EDS mapping analysis of FTP-24. (**d**,**e**) TEM images of FTP-8 and FTP-24 with the lattice fringes in the insert.

Figure 3d,e illustrates the TEM images of FTP-8 and FTP-24. It can be seen that the amorphous layer was uniformly covered on the crystalline phase. The interplanar spacing of intra particles was 2.69 Å, corresponding to the (112) plane of Hematite Fe_2O_3. The thickness of the amorphous coating layer of FTP-8 was about 1–3 nm; however, the thickness increased to 5–8 nm in the FTP-24 sample, which was due to its longer polymerization

duration. Moreover, a double-layer coating structure is observed in Figure 3e, which may be attributed to the TiO_{2-x} and PEDOT layer.

3.2. Electrochemical Performance of the Compounds

The cyclic voltammogram results are shown in Figure 4. For the FTP samples, the first distinct cathodic peak with a high current density appeared at about 0 to 0.4 V, corresponding to the SEI film formation and irreversible lithiation reaction [43]. The reversible conversion reaction from Fe_2O_3 to the cubic $Li_2(Fe_2O_3)$ and further to Fe^0 took place as well in the first cathodic scanning process. The anodic board peaks, appearing at 1.06 and 1.53 V, can be ascribed to the Fe^0 two-step oxidation to Fe^{2+} and to Fe^{3+}. All the first-cycle curves are illustrated in Figure 4e. As the polymerization duration increased, especially for the FTP-56 sample, the cathodic peaks at 0.4 V became more distinct, indicating a greater irreversible lithiation reaction and more lithium loss occurring in the first cycle. After the first cycle, as shown in Figure 4a–d, the CV curves became stable. The cathodic peak shifted to 0.75 V and the current density was slightly weaker, indicating the reversible lithiation process. The CV curves of bare Fe_2O_3 are shown in Figure 4f. It can be seen that the irreversible reaction peak at 0.61 V was much sharper, signifying more lithium loss in the first cycles for the SEI formation. After the first cycle, the capacity loss was significant, as shown by observing the current density decrease in the first three cycles. Thus, in comparison to the PEDOT-coated samples, the bare Fe_2O_3 exhibited a quite unstable state in the electrochemical process.

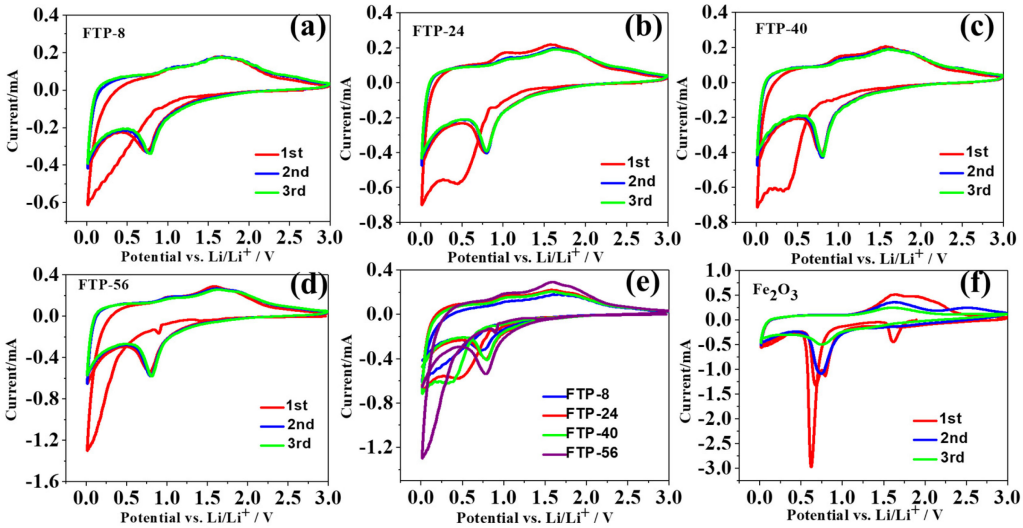

Figure 4. First three cycles of cyclic voltammograms of (**a**) FTP-8, (**b**) FTP-24, (**c**) FTP-40, (**d**) FTP-56, (**e**) first cycle of CV results of all the FTP samples, and (**f**) first three cycles of CV results of bare Fe_2O_3.

The constant current charge–discharge curves (current density, 100 mA/g) of the first three cycles of the obtained samples are illustrated in Figure 5. The optimal one of the FTP samples, FTP-24, was chosen to study the PEDOT coating's effects on the electrochemical performance. The first specific discharge and charge capacities were 1543.4 and 1062.1 mAh/g, respectively, and the corresponding initial coulombic efficiency (ICE) was 68.81%. The results were well-matched to the CV analysis, in which the low ICE was caused by the irreversible lithiation process and the formation of SEI film. In the following cycles, the capacity decay became less noticeable and the electrode exhibited a quite stable charge–discharge plateau. In order to further understand the PEDOT and TiO_2 coatings' synergistic effects on the electrochemical performance, samples without PEDOT (FT), without TiO_2 (FP-24), and without both (Fe_2O_3) were prepared, and their corresponding results are shown in Figure 5b–d, respectively. In the first three cycles of the three samples, the capacity decay was significant, rather than the FTP-24 sample only being significant in the first cycle. In the initial discharge process, there were two typical plateaus at about 1.7 and 0.75 V in the Fe_2O_3@PEDOT-24h and Fe_2O_3 samples, conforming to the CV results. Meanwhile, the plateau at 1.7 V disappeared in the

Fe_2O_3@TiO_2 sample. It is worth noting that the PEDOT coating effectively inhibited the rapid capacity decay, and the stable plateau at 0.75 V remained in the discharge process as well. The initial specific discharge, charge capacity, and Coulombic efficiency of all the FTP samples and control groups are listed in Table 1. It can be seen that the TiO_2 coating was the key factor leading to the decrease in ICE, and PEDOT had a slight positive effect on enhancing the ICE. All the FTP samples possessed a similar ICE, however, FTP-24 showed the highest initial charge–discharge specific capacity. In comparison to the other FTP samples, FTP-24 exhibited a higher capacity retention as well.

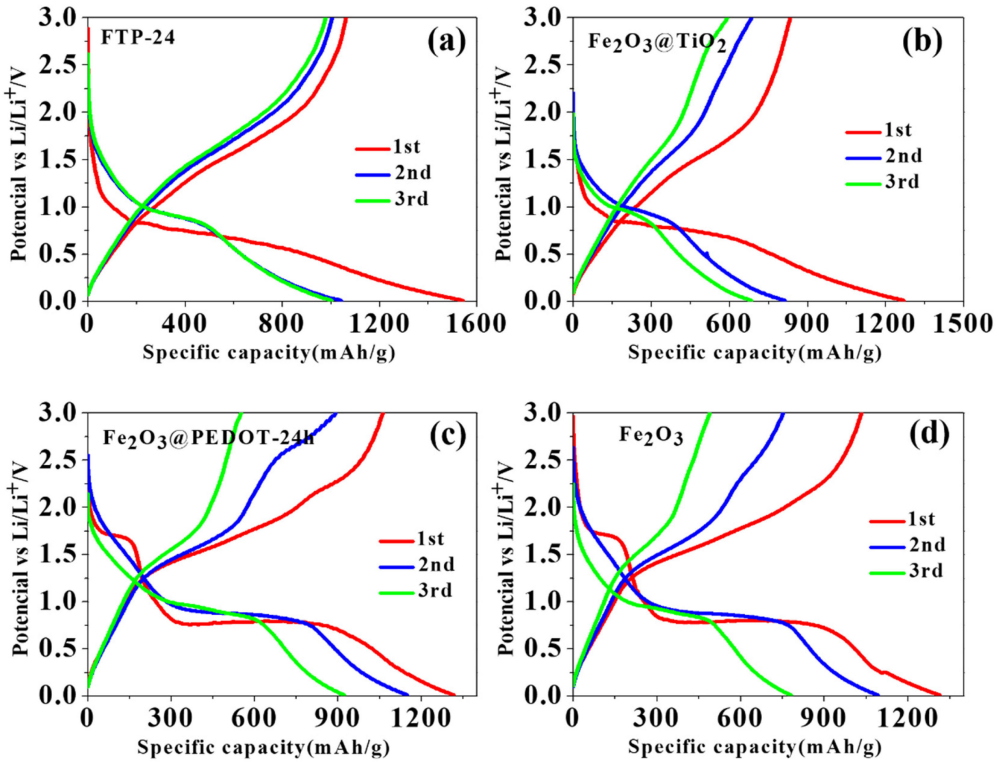

Figure 5. The constant current charge–discharge curves (current density, 100 mA/g) of first three cycles of FTP-24 (**a**), Fe_2O_3@TiO_2 (**b**), Fe_2O_3@PEDOT-24h (**c**), and Fe_2O_3 (**d**).

Table 1. The charge–discharge specific capacity of the initial cycle and the initial coulombic efficiency of all the FTP samples and the control groups at a current of 100 mA/g.

Sample	Initial Charge Specific Capacity (mAh/g)	Initial Discharge Specific Capacity (mAh/g)	Initial Coulombic Efficiency (%)	Charge Capacity after 150 Cycles (mAh/g)	Discharge Capacity after 150 Cycles (mAh/g)
FTP-8	731.1	1107.0	66.04	513.6	518.4
FTP-24	1062.1	1543.4	68.81	623.4	628.2
FTP-40	761.4	1180.1	64.52	433.3	437.6
FTP-56	659.7	986.7	66.86	358.6	356.9
FT	833.6	1269.3	65.67	230.0	228.6
FP-24	1062.5	1318.2	80.60	97.1	97.5
Fe_2O_3	1033.3	1313.8	78.65	75.87	76.0

The cycle performances and impedance spectra are illustrated in Figure 6. The FTP samples, especially FTP-24, exhibited a better cycle performance at 100 mA/g than those without dual-hierarchical decoration, as shown in Figure 6a. This phenomenon was due

to the synergistic effect of the TiO_2 and PEDOT coating on inhibiting the Fe_2O_3 volume change in the charge–discharge process. As a good Li-ion conductor, TiO_2 isolated the direct contact between the Fe_2O_3 and the electrolyte, meanwhile, PEDOT relieved the particle pulverization issue, owing to its flexibility. It was noticed that the FT sample exhibited a lower specific capacity than in our previous report, which was due to the change in the binder. The sodium alginate was proven ineffective when we introduced PEDOT into the samples.

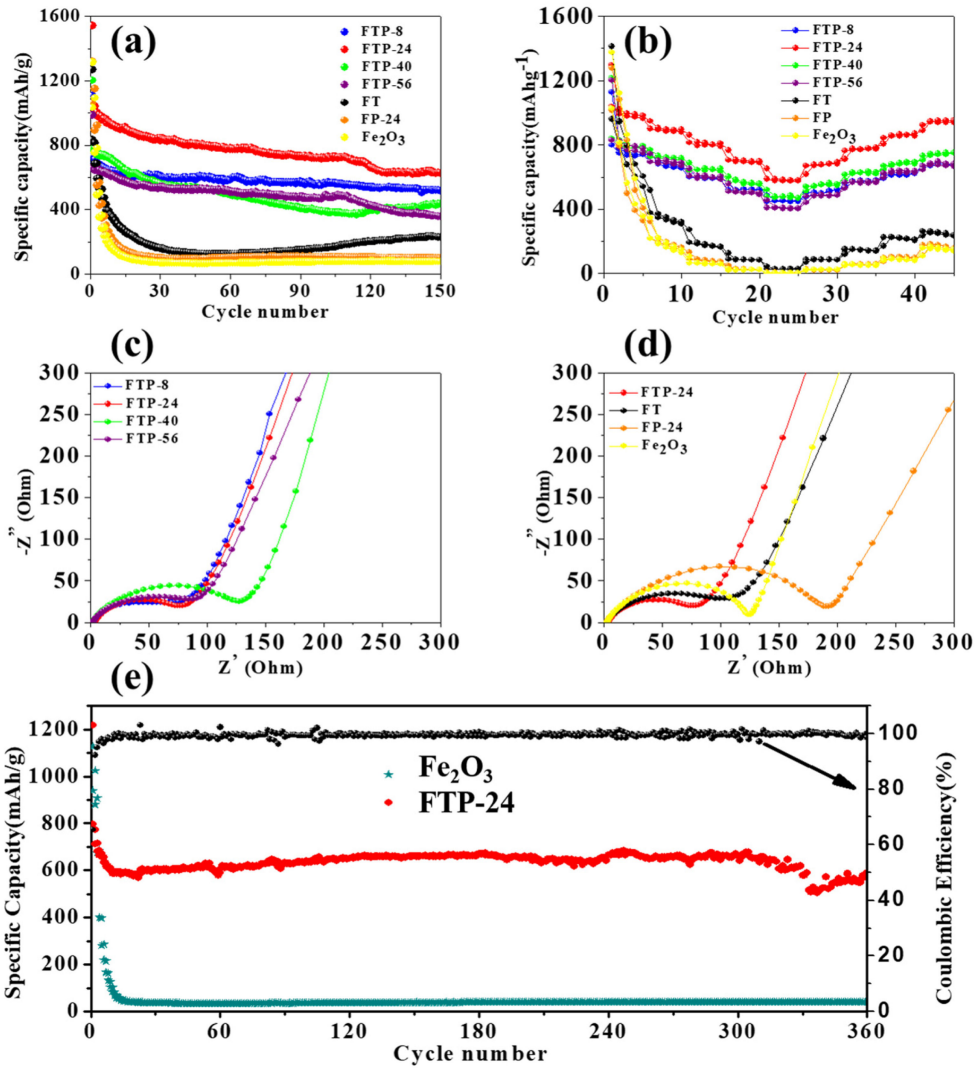

Figure 6. The electrochemical performance of the FTP, FT, FP, and bare Fe_2O_3 samples. (**a**) Cycle performance at a current density of 100 mA/g, (**b**) rate performance, (**c**,**d**) impedance spectra, and (**e**) long cycle performance comparison of FTP-24 and Fe_2O_3, 360 cycles at 100 mA/g.

The rate performance is shown in Figure 6b and current densities of 25, 50, 100, 200, 400, 200, 100, 50, and 25 mA/g were selected. It can be seen that the specific capacity decreased more slightly with an increase in the current density of the FTP samples, especially FTP-24, in comparison to that of the non-FTP samples. The specific capacity recovered to the initial value when the current density was back. The non-FTP samples exhibited fast decay with increasing the current density, even to zero under 400 mA/g. This inferred the dual hierarchical decoration availably improved the ionic and electronic conductivity of the commercial Fe_2O_3 materials.

To further understand the enhancement effect on the ionic and electronic conductivity of the TiO_2 and PEDOT decoration, impedance spectra were performed, as shown in

Figure 6c,d. By comparing the Nyquist plots at a high frequency in Figure 6c, the FTP samples exhibited a low charge transfer resistance (R_{ct}, ~80 Ω), except FTP-40 (~140 Ω), which inferred that more PEDOT coating did not determinately lead to a decrease in transfer resistance. This phenomenon was confirmed by the FP-24 sample, which possessed the highest Rct value (shown in Figure 6d). The results explained that the FTP-40 sample showed a poor cycle performance out of all the FTP samples. In the low-frequency region, the slopes of the spectra were similar to each other, which meant the double-layer coating had slight inhibiting effect on the Li-ion diffusion. In Figure 6d, the FTP sample showed great advantage in reducing the R_{ct}, compared to the single-layer or bare Fe_2O_3, and even the resistance had a significant increase in the single PEDOT-coated sample, which demonstrated that the synergistic effect of the dual coating was quite important. The primary factor contributing to the higher Rct was the interface formed between the PEDOT and Fe_2O_3, imposing constraints on the electron transport. However, by introducing TiO_2 with oxygen defects as an intermediary, we managed to significantly enhance the interfacial contact.

The long cycle performance of the FTP-24 sample is illustrated in Figure 6e. It can be seen that the specific capacity and cycle stability were enhanced significantly by the dual hierarchical decoration, compared to the bare Fe_2O_3.The discharge specific capacity remained at 588.9 mAh/g after 360 cycles at a current density of 100 mA/g. To emphasize the significance of our Fe_2O_3 composites, we include a comparison with other outstanding reported anodes in Table 2. As evident from the table and its long cycle performance, the modified industrial Fe_2O_3 exhibited substantial promise as an anode material for Li-ion batteries.

Table 2. A comparison between our study and previously reported data for reference.

Materials	Current Density (mA/h)	Initial Discharge Specific Capacity (mAh/g)	Reversible Capacity (mAh/g)	Capacity Retention (%)	Ref.
0.2rGO/Fe_2O_3 −175 °C	100	1372	435 (50 Cycles)	31.7	[44]
Fe_3O_4@graphene	100	1625	849 (100 Cycles)	52.2	[45]
Silicon-Carbon	100	1090	200 (100 Cycles)	18.3	[46]
10%-SC	100	1227	800 (100 Cycles)	65.2	[47]
CuO-NiO/rGO	100	990	680 (50 Cycles)	68.7	[48]
Carbon@SnS_2 core–shell microspheres	100	1611	500 (50 Cycles)	31.0	[49]
FTP-24	100	1543	588.9 (360 Cycles)	40.7	This work

4. Conclusions

A facile polymerization method was applied to decorate industrial Fe_2O_3 with a TiO_2 and PEDOT dual coating for application as an anode material in Li-ion batteries. The synergistic effect of the hierarchical layer on the enhancement of cycle stability was demonstrated by the structural and electrochemical characterization. The ceramic-phase TiO_2 isolated the direct contact between the Fe_2O_3 and the electrolyte, meanwhile, PEDOT relieved the particle pulverization issue, owing to its flexibility. The optimum FTP-24 sample, corresponding to a polymerization duration of 24 h, exhibited the most excellent specific capacity and cycle performance. Too long of a polymerization duration would affect the electronic conductivity and Li-ion transportation in the electrode. Due to the dual hierarchical decoration, the composites based on the industrial Fe_2O_3 possessed 588.9 mAh/g after 360 cycles at a current density of 100 mA/g, which could make them excellent candidates as commercial anode materials.

Author Contributions: Conceptualization, Y.M. and G.S.; methodology, Y.X. and T.Y.; software, Q.L.; validation, L.Z., Q.L. and H.L.; formal analysis, Z.C. and Y.M.; investigation, S.W.; resources, G.S.; data curation, J.L.; writing—original draft preparation, Y.M.; writing—review and editing, Y.X., T.Y. and G.S.; visualization, Q.L.; supervision, G.S. and Y.X.; project administration, G.S.; funding acquisition, Y.M. and G.S. All authors have read and agreed to the published version of the manuscript.

Funding: This work was supported by Natural Science Foundation of China (No. 52207246), Key projects of natural science research in universities of Anhui Province (KJ2020A0263), Anhui Natural Science Foundation (No. 1908085ME151), and China Postdoctoral Science Foundation (No. 2020M673404). We are also grateful to the open project (Key Lab Marine Mat & Related Technol, CAS, 2019K07; State Key Lab of Advanced Special Steel, Shanghai Key Lab of Adv. Ferrometallurgy SKLASS 2019-23) for providing some characterization support.

Data Availability Statement: The data presented in this study are available on request from the corresponding author. The data are not publicly available due to privacy.

Conflicts of Interest: The authors declare no conflict of interest.

References

1. Ding, B.; Ding, M.; Ma, Y.; Song, G.; Li, Z.; Ge, J.; Yang, W.; Wen, C. Effect of MgO on electrochemical properties of silicon-based anode composite material. *Solid State Sci.* **2022**, *131*, 106940. [CrossRef]
2. Wei, T.; Zhang, N.; Ji, Y.; Zhang, J.; Zhu, Y.; Yi, T. Nanosized zinc oxides-based materials for electrochemical energy storage and conversion: Batteries and supercapacitors. *Chin. Chem. Lett.* **2022**, *33*, 714–729. [CrossRef]
3. Xu, L.; Chon, M.J.; Mills, B.; Thompson, C.V. Mechanical stress and morphology evolution in RuO_2 thin film electrodes during lithiation and delithiation. *J. Power Sources* **2022**, *552*, 232260. [CrossRef]
4. Xu, L.; Thompson, C.V. Mechanisms of the cyclic (de)lithiation of RuO_2. *J. Mater. Chem. A* **2020**, *8*, 21872–21881. [CrossRef]
5. Huang, Y.; Li, Q.; Wang, S.; Cai, Z.; Ma, Y.; Song, G.; Yang, W.; Wen, C.; Xie, Y. Enhanced electrochemical performance of silicon anode materials with titanium hydride treatment. *J. Electroanal. Chem.* **2023**, *933*, 117292. [CrossRef]
6. Gu, Z.Y.; Heng, Y.L.; Guo, J.Z.; Cao, J.M.; Wang, X.T.; Zhao, X.X.; Sun, Z.H.; Zheng, S.H.; Liang, H.J.; Li, B.; et al. Nano self-assembly of fluorophosphate cathode induced by surface energy evolution towards high-rate and stable sodium-ion batteries. *Nano Res.* **2023**, *16*, 439–448. [CrossRef]
7. Du, K.D.; Meng, Y.F.; Zhao, X.X.; Wang, X.T.; Luo, X.X.; Zhang, W.; Wu, X.L. A unique co-recovery strategy of cathode and anode from spent $LiFePO_4$ battery. *Sci. China Mater.* **2022**, *65*, 637–645. [CrossRef]
8. Zhang, K.Y.; Gu, Z.Y.; Ang, E.H.; Guo, J.Z.; Wang, X.T.; Wang, Y.; Wu, X.L. Advanced polyanionic electrode materials for potassium-ion batteries: Progresses, challenges and application prospects. *Mater. Today* **2022**, *54*, 189–201. [CrossRef]
9. Xu, X.; Li, F.; Zhang, D.; Ji, S.; Huo, Y.; Liu, J. Facile construction of $CoSn/Co_3Sn_2$@C nanocages as anode for superior lithium-/sodium-ion storage. *Carbon Neutralization* **2023**, *2*, 54–62. [CrossRef]
10. Bai, Y.; Muralidharan, N.; Sun, Y.K.; Passerini, S.; Stanley Whittingham, M.; Belharouak, I. Energy and environmental aspects in recycling lithium-ion batteries: Concept of Battery Identity Global Passport. *Mater. Today* **2020**, *41*, 304–315. [CrossRef]
11. Qu, X.; Huang, H.; Wan, T.; Hu, L.; Yu, Z.; Liu, Y.; Dou, A.; Zhou, Y.; Su, M.; Peng, X.; et al. An integrated surface coating strategy to enhance the electrochemical performance of nickel-rich layered cathodes. *Nano Energy* **2022**, *91*, 106665. [CrossRef]
12. Liu, D.; Fan, X.; Li, Z.; Liu, T.; Sun, M.; Qian, C.; Ling, M.; Liu, Y.; Liang, C. A cation/anion co-doped $Li_{1.12}Na_{0.08}Ni_{0.2}Mn_{0.6}O_{1.95}F_{0.05}$ cathode for lithium ion batteries. *Nano Energy* **2019**, *58*, 786–796. [CrossRef]
13. Cai, Z.; Wang, S.; Zhu, H.; Tang, X.; Ma, Y.; Yu, D.Y.W.; Zhang, S.; Song, G.; Yang, W.; Xu, Y.; et al. Improvement of stability and capacity of Co-free, Li-rich layered oxide $Li_{1.2}Ni_{0.2}Mn_{0.6}O_2$ cathode material through defect control. *J. Colloid Interface Sci.* **2023**, *630*, 281–289. [CrossRef] [PubMed]
14. Sun, M.; Chu, X.; Wang, Z.; Yang, H.; Yang, Z.; Ma, J.; Zhou, B.; Yang, T.; Chen, L. Rosa roxburghii-like hierarchical hollow sandwich-structure C@Fe_2O_3@C microspheres as second nanomaterialsfor superior lithium storage. *J. Alloys Compd.* **2021**, *855*, 157518. [CrossRef]
15. Ding, B.; Cai, Z.; Ahsan, Z.; Ma, Y.; Zhang, S.; Song, G.; Yuan, C.; Yang, W.; Wen, C. A Review of Metal Silicides for Lithium-Ion Battery Anode Application. *Acta Metall. Sin.* **2021**, *34*, 291–308. [CrossRef]
16. Li, F.; Wang, Z.; Liu, W.; Yan, T.; Zhai, C.; Wu, P.; Zhou, Y. Double-Network Gel-Enabled Uniform Incorporation of Metallic Matrices with Silicon Anodes Realizing Enhanced Lithium Storage. *ACS Appl. Energy Mater.* **2019**, *2*, 2268–2275. [CrossRef]
17. Fang, R.; Xiao, W.; Miao, C.; Mei, P.; Zhang, Y.; Yan, X.; Jiang, Y. Enhanced lithium storage performance of core-shell structural Si@TiO_2/NC composite anode via facile sol-gel and in situ N-doped carbon coating processes. *Electrochim. Acta* **2019**, *317*, 575–582. [CrossRef]
18. Zhong, H.; Huang, W.; Wei, Y.; Yang, X.; Jiang, C.; Liu, H.; Zhang, W.; Liang, C.; Dai, L.; Xu, X. Facile Constructing Hierarchical Fe_3O_4@C Nanocomposites as Anode for Superior Lithium-Ion Storage. *Batteries* **2023**, *9*, 403. [CrossRef]
19. Reddy, M.V.; Yu, T.; Sow, C.H.; Shen, Z.X.; Lim, C.T.; Rao, G.V.S.; Chowdari, B.V.R. α-Fe_2O_3 nanoflakes as an anode material for li-ion batteries. *Adv. Funct. Mater.* **2007**, *17*, 2792–2799. [CrossRef]

20. Liu, H.; Zhu, J.; Li, Z.; Shi, Z.; Zhu, J.; Mei, H. Fe_2O_3/N doped rGO anode hybridized with NiCo LDH/$Co(OH)_2$ cathode for battery-like supercapacitor. *Chem. Eng. J.* **2021**, *403*, 126325. [CrossRef]
21. Hwang, J.; Yadav, D.; Yang, H.; Jeon, I.; Yang, D.; Seo, J.W.; Kang, M.; Jeong, S.Y.; Cho, C.R. In Situ Electrochemical Impedance Measurements of α-Fe_2O_3 Nanofibers: Unravelling the Li-Ion Conduction Mechanism in Li-Ion Batteries. *Batteries* **2022**, *8*, 44. [CrossRef]
22. Liu, Y.; Lei, J.; Chen, Y.; Liang, C.; Ni, J. Hierarchical-Structured Fe_2O_3 Anode with Exposed (001) Facet for Enhanced Lithium Storage Performance. *Nanomaterials* **2023**, *13*, 2025. [CrossRef] [PubMed]
23. Lai, H.; Li, J.-Q.; Lin, Y.-Y.; Sun, Y.-H. Flower-like multi-shells MO/Fe_2O_3 (M = Cu, Mn and Ni) hollow microspheres for lithium ion battery with super cycle stability. *Inorg. Chem. Commun.* **2023**, *154*, 110947. [CrossRef]
24. Li, J.; Yan, L. Synthesis of Fe_2O_3/rGO Based Composites as Anode material for Lithium ion batteries using sewage sludge as source of Iron (III) oxide. *Int. J. Electrochem. Sci.* **2022**, *17*, 221173. [CrossRef]
25. Pan, Y.; Luo, C.; Yang, D.; Sun, P.; Chen, J.; Sui, Z.; Tian, Q. Ultrathin porous Fe_2O_3@C nanosheets: Novel preparation strategy and high lithium storage. *Appl. Surf. Sci.* **2023**, *635*, 157763. [CrossRef]
26. Ge, Y.; Gao, W.; Yuan, Z.; Tao, S.; Kong, F.; Qian, B. Synergistic effect on the improved lithium ion storage performance in the porous Fe_2O_3@Fe_3C@C composite. *Mater. Res. Bull.* **2023**, *164*, 112287. [CrossRef]
27. Xu, Z.; Sun, M.; Wu, S.; Chen, Y.; Li, L.; Zou, X.; Chen, L.; Yang, H.; Pang, H. Interfacial engineering of graphene aerogel encapsulated $FeSe_2$-Fe_2O_3 heterojunction nanotubes for enhanced lithium storage. *J. Alloys Compd.* **2023**, *934*, 167939. [CrossRef]
28. Jin, Y.; Zhang, W.; Qing, T.; Chen, G.; Zeng, S.; Huang, J. Constructing 3D sandwich-like carbon coated Fe_2O_3/helical carbon nanofibers composite as a superior lithium-ion batteries anode. *J. Electroanal. Chem.* **2023**, *929*, 117098. [CrossRef]
29. Chen, L.; Zhao, C.; Lu, Y.; Wan, L.; Yan, K.; Bai, Y.; Liu, Z.; Yang, X.; Su, Y.; Wu, F. Facile Synthesizing Yolk-Shelled Fe_3O_4@Carbon Nanocavities with Balanced Physiochemical Synergism as Efficient Hosts for High-Performance Lithium–Sulfur Batteries. *Batteries* **2023**, *9*, 295. [CrossRef]
30. Shi, W.C.; Shao, Y.R.; Shen, Y.; Li, Z.F.; Hu, T.L. Facile synthesis of porous iron oxides heterostructural nanosheets as an enhanced anode material for lithium ion battery. *Mater. Lett.* **2022**, *321*, 132454. [CrossRef]
31. Zhu, J.; Wei, L.; Hu, J.; Xue, C. Anchoring iron oxide nanoparticles on polypyrrole/rGO derived nitrogen-doped carbon as lithium-ion battery anode. *J. Alloys Compd.* **2017**, *723*, 729–735. [CrossRef]
32. Zheng, Z.; Li, P.; Huang, J.; Liu, H.; Zao, Y.; Hu, Z.; Zhang, L.; Chen, H.; Wang, M.S.; Peng, D.L.; et al. High performance columnar-like Fe_2O_3@carbon composite anode via yolk@shell structural design. *J. Energy Chem.* **2020**, *41*, 126–134. [CrossRef]
33. Qin, G.; Zeng, M.; Wu, X.; Wen, J.; Li, J. Fabrication of Fe_2O_3@TiO_2 core–shell nanospheres as anode materials for lithium-ion batteries. *J. Mater. Sci. Mater. Electron.* **2018**, *29*, 12944–12950. [CrossRef]
34. Ma, Y.; Zhang, L.; Cai, Z.; Huang, X.; Ding, B.; Ahsan, Z.; Song, G.; Xu, Y.; Yang, W.; Wen, C. Study of TiO_2 -Coated α-Fe_2O_3 Composites and the Oxygen-Defects Effect on the Application as the Anode Materials of High-Performance Li-Ion Batteries. *ACS Appl. Energy Mater.* **2020**, *3*, 11666–11673. [CrossRef]
35. Fu, Y.; Wei, Q.; Lu, B.; Wang, X.; Sun, S. Stem-like nano-heterostructural MWCNTs/α-Fe_2O_3@TiO_2 composite with high lithium storage capability. *J. Alloys Compd.* **2016**, *684*, 419–427. [CrossRef]
36. Zhu, J.; Xu, Y.; Wang, J.; Wang, J.; Bai, Y.; Du, X. Morphology controllable nano-sheet polypyrrole-graphene composites for high-rate supercapacitor. *Phys. Chem. Chem. Phys.* **2015**, *17*, 19885–19894. [CrossRef] [PubMed]
37. Zeng, Y.; Xie, D.; Ai, S.; Huang, H.; Zheng, Z.; Xie, S.; Liu, P.; Wang, S.; Zhang, M.; Cheng, F. Facile fabrication of core-shell α-Fe_2O_3@PPy imbedded into porous biomass-derived carbon for enhanced lithium storage. *J. Energy Storage* **2023**, *67*, 107625. [CrossRef]
38. Rasool, M.; Chiu, H.C.; Zank, B.; Zeng, Y.; Zhou, J.; Zaghib, K.; Perepichka, D.F.; Demopoulos, G.P. PEDOT Encapsulated and Mechanochemically Engineered Silicate Nanocrystals for High Energy Density Cathodes. *Adv. Mater. Interfaces* **2020**, *7*, 202000226. [CrossRef]
39. da Silva, R.J.; Lima, R.M.A.P.; de Oliveira, M.C.A.; Alcaraz-Espinoza, J.J.; de Melo, C.P.; de Oliveira, H.P. Supercapacitors based on (carbon nanostructure)/PEDOT/(eggshell membrane) electrodes. *J. Electroanal. Chem.* **2020**, *856*, 113658. [CrossRef]
40. Jeong, J.M.; Choi, B.G.; Lee, S.C.; Lee, K.G.; Chang, S.J.; Han, Y.K.; Lee, Y.B.; Lee, H.U.; Kwon, S.; Lee, G.; et al. Hierarchical hollow spheres of Fe_2O_3@polyaniline for lithium ion battery anodes. *Adv. Mater.* **2013**, *25*, 6250–6255. [CrossRef]
41. Chen, H.W.; Li, C. PEDOT: Fundamentals and Its Nanocomposites for Energy Storage. *Chin. J. Polym. Sci.* **2020**, *38*, 435–448. [CrossRef]
42. Wu, C.; Chen, J.; Liang, L.; Li, N. N-doped/oxygen-deficient Fe_2O_3-x @PEDOT cruciform nanosheet arrays: Boosting the performance of all-solid-state flexible supercapacitors. *Chem. Phys. Lett.* **2023**, *823*, 2–6. [CrossRef]
43. Chaudhari, S.; Srinivasan, M. 1D hollow α-Fe_2O_3 electrospun nanofibers as high performance anode material for lithium ion batteries. *J. Mater. Chem.* **2012**, *22*, 23049–23056. [CrossRef]
44. Zhu, G.; Gao, B.; Tu, G.; Liu, H.; Wang, M. Improving Effect of Graphene on Electrochemical Properties of Fe_2O_3 Anode Materials. *Metals* **2022**, *12*, 593. [CrossRef]
45. Suo, Y.; Zhao, Q.Q.; Meng, J.K.; Li, J.; Zheng, X.C.; Guan, X.X.; Liu, Y.S.; Zhang, J.M. Fabrication and electrochemical properties of 3D Fe_3O_4@graphene aerogel composites as lithium-ion battery anodes. *Mater. Lett.* **2016**, *174*, 36–39. [CrossRef]
46. Shen, L.; Wang, D.; Ali, K.; Li, M.; Shi, Z. Electrochemical Preparation of Nano-Sized Silicon as a Lithium-Ion Battery Anode Material. *J. Electrochem. Soc.* **2021**, *168*, 120509. [CrossRef]

47. Jiang, J.; Ou, Y.; Jiang, Y.; Hu, X.; Xing, C.; Liu, S.; Liu, X.; Li, W.; Zhao, B. Preparation of SiOx–TiO_2/Si/CNTs composite microspheres as novel anodes for lithium-ion battery with good cycle stability. *J. Mater. Sci. Mater. Electron.* **2022**, *33*, 11025–11037. [CrossRef]
48. Ranjbar-Azad, M.; Behpour, M. Facile in situ co-precipitation synthesis of CuO–NiO/rGO nanocomposite for lithium-ion battery anodes. *J. Mater. Sci. Mater. Electron.* **2021**, *32*, 18043–18056. [CrossRef]
49. Yu, G.; Chen, X.; Wang, A.; Wang, Y. Carbon@SnS_2 core-shell microspheres for lithium-ion battery anode materials. *Ionics* **2018**, *24*, 2915–2923. [CrossRef]